

# Towards Integrated Design of a Robust Feedback Controller and Topography Estimator for Atomic Force Microscopy

Stefan Kuiper\* Paul M.J. Van den Hof\* Georg Schitter\*\*

\* *Delft Center for Systems and Control, Delft University of  
Technology, Mekelweg 2, 2628CD Delft, The Netherlands (e-mail:  
stefan.kuiper@tudelft.nl, p.m.j.vandenhof@tudelft.nl).*

\*\* *Automation and Control Institute, Vienna University of Technology,  
Gusshausstrasse 27-29, 1040 Vienna, Austria. (e-mail:  
schitter@acin.tuwien.ac.at)*

---

Abstract: In Atomic Force Microscopy (AFM), the force between the measurement tip and the sample is controlled in a feedback loop to prevent damage to the tip and sample during imaging, and to convert the measurement of the tip-sample force into an estimation of the sample topography. Dynamical uncertainties of the system pose a strong limitation on the achievable control bandwidth, and on the accuracy of the estimated topography. This contribution discusses an integrated approach to design a robust feedback controller and topography estimator, taking into account the dynamical uncertainties of the imaging system. It is shown that for a given AFM system there exist a direct trade-off between the closed-loop bandwidth and the guaranteed bounds on the topography estimation error due to the dynamic uncertainties in the system.

*Keywords:* High-speed AFM, dual-actuation, robust control, topography estimation

---

## 1. INTRODUCTION

Atomic Force Microscopy (AFM) [Binnig et al. (1986)] is an important tool in micro-, and nano-technology to provide images of sample topography with molecular or even atomic resolution [Sarid (1994)]. In AFM, the sample topography is measured by probing the sample with a very sharp tip, while scanning the sample or tip in a raster scan-pattern. The measurement tip is mounted on the free end of a micro-cantilever which allows to measure the interaction force between the tip and the sample during imaging. The tip-sample interaction force is controlled in a feedback loop, manipulating the distance between the tip and sample. The purpose of this vertical feedback loop is twofold: to prevent damage of the tip and the sample during imaging, and to provide an estimate of the sample topography. In order to provide the scanning motion and to allow the control of the tip-sample force, a positioning stage is used which can position the tip relative to the sample in all three spatial directions.

Although AFM is capable of providing high resolution topography images in a wide range of applications and environmental conditions, one of its main limitations is its low imaging speed [Hansma et al. (2006)]. In order to improve the imaging speed of AFM, a vast amount of research has been done on improving both the mechanical design of the AFM-system [Ando et al. (2001); Schitter et al. (2007)], as well as improved control of the scanning motion [Devasia et al. (2007); Butterworth et al. (2009)], and improved control of the tip-sample interaction force [Schitter et al. (2001); Salapaka et al. (2005)]. Nowadays, prototype high speed AFM-systems have been reported, allowing scan-

rates of more than 1000 lines per second [Ando et al. (2001); Picco et al. (2007); Schitter et al. (2007)]. The main limitation on the imaging speed, however, is considered the closed-loop bandwidth of the vertical feedback loop [Hansma et al. (2006)]. Recently, dual actuated control schemes are proposed, allowing a significant increase of the closed-loop bandwidth of the vertical feedback loop without sacrificing effective positioning range, by using a combination of a long-range, low-bandwidth actuator and a short-range, high-bandwidth actuator [Sulchek et al. (1999)].

Although a lot of research has gone into increasing the bandwidth of both the scanning-stage as well as the vertical feedback-loop, the consequences of the higher control bandwidths on the accuracy of the topography measurement has not been investigated in much detail. In [Schitter et al. (2001)] improved topography estimation is discussed by taking into account a model of the dynamical behavior of the system. In [Salapaka et al. (2005)] it is shown how the estimator model can be incorporated in the feedback controller design. The dynamical behavior of the system, however, may show some variations when changing the tip or sample, which poses strong limitations on the achievable control bandwidth and the accuracy of the topography estimation. In this contribution an integrated design method for the feedback controller and topography estimator is discussed, taking into account the dynamical uncertainties of the system.

In Section 2 the topography estimation problem is explained and how the accuracy of the topography estimation depends on the dynamical uncertainty of the system. An integrated approach to design a feedback controller

and topography estimator is presented in Section 3, taking into account the dynamical uncertainties of the system. Application of this design approach to a prototype dual actuated AFM is discussed and analyzed in Section 4, and conclusions are drawn in Section 5.

## 2. TOPOGRAPHY ESTIMATION PROBLEM

Figure 1 shows a block diagram of the vertical feedback loop in AFM, with  $G$  the actuator dynamics,  $P$  the sensor dynamics, and  $K$  the feedback controller. While scanning, the sample topography enters the feedback loop as an unknown disturbance signal denoted  $h(t)$  in Figure 1, which in the Laplace domain is given as:

$$H(s) = \underbrace{\frac{1}{1+L(s)} \cdot H(s)}_{E(s)} + \underbrace{\frac{L(s)}{1+L(s)} \cdot H(s)}_{-X(s)}, \quad (1)$$

with  $L(s) = P(s) \cdot K(s) \cdot G(s)$  the loop gain of the control loop.  $H(s)$ ,  $X(s)$  and  $E(s)$  are the Laplace transforms of the topography signal  $h(t)$ , the actuator displacement  $x(t)$ , and the control error  $e(t)$  respectively.

The objective of the vertical feedback loop is twofold: prevent damage and wear of the measurement tip and sample by minimizing the control error  $e(t) = x(t) + h(t)$ , and minimizing the topography estimation error  $\epsilon(t) = \hat{h}(t) - h(t)$ .

In high accuracy metrological AFM-systems, the sample topography is measured by directly measuring the actuator displacement  $x(t)$  with high accuracy displacement sensors (e.g. interferometric). When assuming that the vertical feedback loop is fast enough to track the sample topography variations while scanning (i.e.  $e(t) \approx 0$ ), the measurement of the actuator displacement can be regarded as a direct measure of the sample topography. The assumption of zero control error, however, only holds when scanning relatively slowly, allowing the feedback control loop sufficient time to recover from topography variations. At higher imaging speeds part of the topography information will enter the control error-signal  $e(t)$ , which should therefore also be taken into account when providing an estimate of the sample topography. As the loop-gain  $L(s)$  typically contains an integral control action to achieve zero steady state error, the actuator displacement  $x(t)$  generally contains low-frequency topography information, while the control error signal  $e(t)$  contains high-frequency topography information (cf. Eqn. (1)). Therefore, most often both the measured control error and the actuator displacement are presented in separate images for each experiment.

For AFM-systems used for qualitative imaging applications the precision of the topography estimation is most important in order to achieve the (sub-)nanometer imaging resolution. However, as opposed to metrological AFM, the required accuracy for AFM systems used for qualitative imaging is not such high and the use of high accuracy displacement sensors to measure the actuator displacement is therefore not very cost-efficient. Moreover, the sensor noise of the position sensors might degrade the measurement precision, which becomes more severe at higher imaging bandwidths as with high-speed AFM. In most commercially available AFM-systems the sample topography is estimated based on the measured control error signal  $d(t)$  and the control signal  $u(t)$  (cf. Fig. 1), which in Laplace domain becomes:

$$\hat{H}(s) = \underbrace{\hat{P}^{-1}(s) \cdot D(s)}_{\hat{E}(s)} - \underbrace{\hat{G} \cdot U(s)}_{\hat{X}(s)}, \quad (2)$$

with  $\hat{P}(s)$  a model of the sensor dynamics  $P(s)$ , and  $\hat{G}(s)$  a model of the actuator dynamics  $G(s)$ . Combining (1) and (2), the topography estimation error can be calculated as:

$$\begin{aligned} \epsilon(s) &= [\hat{E}(s) - E(s)] - [\hat{X}(s) - X(s)] \\ &= [\hat{P}(s)^{-1} \cdot D(s) - E(s)] - [\hat{G}(s) \cdot U(s) - X(s)] \\ &= \frac{[P(s)\hat{P}^{-1}(s) - 1] - P(s)K(s) [\hat{G}(s) - G(s)]}{1 + L(s)} \cdot H(s), \quad (3) \end{aligned}$$

i.e. topography estimation error is partly stemming from the modeling error of the sensor dynamics  $[P(s) \cdot \hat{P}^{-1}(s) - 1]$ , and partly stemming from the modeling error of the actuator dynamics  $[\hat{G}(s) - G(s)]$ . Important is also to note the influence of the loop gain  $L(s)$  and the feedback controller  $K(s)$  in (3), determining the propagation of the modeling errors towards the topography estimation error.

In dynamic mode AFM, the cantilever dynamics in  $P$  are non-linear, making it difficult to identify and capture in a model. Therefore, in dynamic mode AFM one strongly relies on the actuator displacement  $x(t)$  as a measure for the sample topography, presuming a good linearization effect of the feedback loop. Recently, however, estimator based techniques are developed which can provide a direct estimate of the control error in dynamic mode AFM [Jeong et al. (2006)]. In contact-mode AFM, the cantilever dynamics can be regarded fairly linear [Schitter et al. (2001)]. The sensor dynamics  $P$  can therefore be regarded as a static gain, which can be identified before each imaging experiment by measuring a force curve [Sarid (1994)].

In conventional AFM-systems, the actuator dynamics  $G(s)$  are approximated by a static gain, of which the value is obtained by calibration. In high-speed AFM-systems, however, the bandwidth of the feedback loop is pushed close to the resonance frequencies of the actuators, such that also the actuator dynamics must be taken into account in the model  $\hat{G}(s)$  [Schitter et al. (2001)]. A difficulty hereby is that the dynamical behavior of the actuator might show some variations when changing the measurement probe and sample mass [van Hulzen et al. (2009)]. Although it is possible to identify the actuator dynamics before each imaging experiment, this is not desirable as the identification experiments are time-consuming, require special expertise, and might also cause damage to the tip and or the sample. Therefore, in this contribution a robust design of the feedback controller and the topography estimator is considered, taking into account the dynamical uncertainties of the system in order to guarantee certain performance specifications with all potentiality used samples and measurement probes.

## 3. ROBUST DESIGN OF FEEDBACK CONTROLLER AND TOPOGRAPHY ESTIMATOR

The primary goal of the feedback controller  $K(s)$  is to control the tip-sample force while imaging. However, from (3) it can be seen that feedback controller  $K(s)$  also has a strong influence on the propagation of the modeling errors towards the topography estimation error. For the design of the feedback controller it is therefore important not only to consider the disturbance rejection problem, but also the topography estimation problem. In this section,

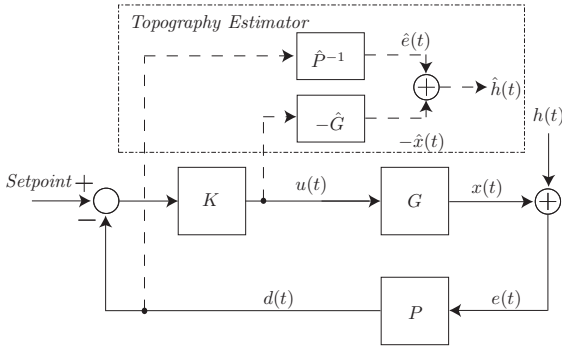


Figure 1. Block diagram of the vertical feedback loop in AFM. With actuator dynamics  $G$ , sensor dynamics  $P$ , and feedback controller  $K$ . The topography estimator provides an estimate of the topography signal  $\hat{h}(t)$  based on sensor signal  $d(t)$  and control signal  $u(t)$ .

an integrated approach is presented to design the feedback controller and topography estimator, taking into account the dynamical variations of the system when using different measurement probe and samples. For simplicity, in the following only contact-mode imaging is considered in which the sensor dynamics  $P$  are assumed to be linear and fully known. However, most of the considerations also hold for dynamic mode AFM. Also the influence of potential system or measurement noise is not considered. Hence, only the modeling error of the actuator dynamics are considered as a potential source of topography estimation errors. The integrated design approach consists of three steps, which are discussed in the following subsections.

### 3.1 Step 1: Identification and modeling of the actuator dynamics

The dynamics of the vertical actuator in AFM can be identified by driving the actuator with an identification signal and measuring the cantilever deflection, while disabling the lateral scanning motion. In order to identify the dynamical behavior of the system under all working conditions, the measurement can be repeated with different samples weights and measurement probes, which all together should give a good and complete resemblance of how the system might be used in practise. Based on the identification data of the various measurement trails, a nominal model and dynamical uncertainty set can be fitted capturing the dynamical behavior of the system with all possible combinations of measurement probes and samples:

$$\mathcal{G} = \{G_{nom}(s) \cdot (1 + \Delta(s)Q(s)), \|\Delta(s)\|_{\infty} \leq 1\}, \quad (4)$$

with  $G_{nom}(s)$  a parametric model of the nominal actuator dynamics, and weighting filter  $Q(s)$  and uncertain parameter  $\Delta(s)$  capturing the dynamical variations of the system. To minimize the conservatism of the model, the nominal model can be obtained by first determining the optimal un-parameterized response of the nominal model at each frequency point which minimizes the worst-case model error:

$$\Gamma(\omega_f) = \arg \min_{\Gamma(\omega_f)} \max_{k=1 \dots n} |\Phi_k(\omega_f) - \Gamma(\omega_f)|, \quad (5)$$

with  $\Phi_k(\omega_f)$  the vectors containing the frequency response data from the various measurement trails. Based on the optimal un-parameterized nominal response  $\Gamma(\omega_f)$ , a parameterized nominal model  $G_{nom}(\omega)$  can be obtained by data

fitting techniques [Pintelon and Schoukens (2001)]. Given the parameterized nominal model and the identification data from the various measurement trails, the worst-case multiplicative modeling error can be determined at each frequency point:

$$\Psi(\omega_f) = \max_{k=1 \dots n} \left| \frac{\Phi_k(\omega_f) - G_{nom}(\omega_f)}{G_{nom}(\omega_f)} \right|. \quad (6)$$

The maximum multiplicative modeling error  $\Psi(\omega_f)$  can be incorporated in the set (4), via a parameterized over-bounding function  $Q(\omega_f) \geq \Psi(\omega_f)$ . Although in this research a multiplicative modeling error description is used, other modeling error descriptions might be used as well (e.g. additive). In choosing a type of modeling error description it should be taken into account how tightly this modeling error description can be over-bounded by the finite order over-bounding function  $Q(\omega)$  [Douma and Van den Hof (2005)]. A too loose over-bounding function might lead to additional conservatism in the model set.

### 3.2 Step 2: Model-based feedback controller design

Based on the model (4), a feedback controller can be designed which guarantees certain  $\mathcal{H}_{\infty}$ -norm bounded performance specifications, using the mixed-sensitivity framework and  $\mu$ -synthesis [Skogestad and Postlethwaite (2005)]. Note that based on the model of (4), the optimal topography estimator would equal the parametric nominal model  $G_{nom}(s)$ , as this model is in the center of the set, and therefore minimizes the worst-case topography estimation error based on that set. With this assumption, and assuming that the cantilever dynamics  $P$  are fully known and linear, i.e.  $P \cdot \hat{P}^{-1} = 1$ , the topography estimation error of (3) becomes:

$$\begin{aligned} \varepsilon(s) &= \frac{K(s) \cdot [G_{nom}(s) - G_{nom}(s)(1 + Q(s)\Delta(s))]}{1 + L(s, \Delta)} \cdot H(s) \\ &= \frac{K(s) \cdot [G_{nom}(s) \cdot Q(s) \cdot \Delta(s)]}{1 + L(s, \Delta)} \cdot H(s), \end{aligned} \quad (7)$$

i.e. the topography estimation error is directly stemming from the excitation of the uncertain dynamics of the system. The feedback controller design problem can therefore be casted in the mixed-sensitivity framework as depicted in Figure 2, with weighting filters  $W_{es}(s)$ ,  $W_e(s)$ , and  $W_u(s)$ , which penalize the topography estimation error  $\varepsilon(t)$ , the control error  $e(t)$ , and the controller output  $u(t)$ , respectively. The objective of the controller synthesis is formulated as finding the controller parameters  $\theta$ , which minimize the worst case  $\mathcal{H}_{\infty}$ -norm of the system:

$$\gamma \geq \min_{\theta} \max_{\Delta} \left\| \begin{array}{c} W_e(s) \cdot S(s, \theta, \Delta) \\ W_u(s) \cdot K(s, \theta) \cdot S(s, \theta, \Delta) \\ W_{es} \cdot \Delta \cdot Q(s) \cdot G_n(s) \cdot K(s, \theta) \cdot S(s, \theta, \Delta) \end{array} \right\|_{\infty}, \quad (8)$$

which can be solved using the  $DK$ -iteration method. The desired behavior of the closed-loop system resulting from the controller synthesis can be enforced via the weighting filters. If after synthesis a value  $\gamma \leq 1$  is achieved, it can be said that for all possible plants in the set (4) the performance criterions governed by the weighting filters are met, and the robust stability is guaranteed [Skogestad and Postlethwaite (2005)].

### 3.3 Step 3: Estimator design

The task of the estimator model  $\hat{G}(s)$  is to estimate the actuator displacement  $x(t)$  based on the measured feedback

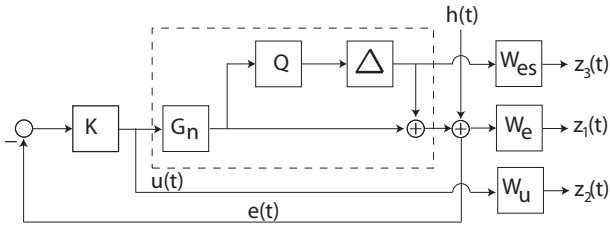


Figure 2. System description for design of the robust feedback control and topography estimator, with input  $h(t)$ , and performance channel-outputs  $z_1(t)$ ,  $z_2(t)$  and  $z_3(t)$

controller output  $u(t)$ , in order to construct an estimation of the sample topography (cf. Fig. 1). The estimator model should be designed in such a way that the worst-case estimation error over all possible system variations is minimized. The estimator dynamics therefore ideally follow the behavior of the un-parameterized nominal model  $\Gamma(\omega_f)$  (cf. Eqn. (5)), which is at the center of set of measured frequency responses. However, to allow implementation of the estimator a parameterized model is required which can be fitted based on  $\Gamma(\omega_f)$ , using for instance least squares data fitting methods [Pintelon and Schoukens (2001)].

The design of the estimator model can also be directly incorporate in the design of the feedback controller, as discussed for nominal controller and estimator design in [Salapaka et al. (2005)]. However, as opposed to the feedback controller, the estimator is not required to run in real-time allowing higher computational complexity. The order of the estimator model can therefore be chosen higher as the model used for the controller synthesis, which may in turn improve the modeling accuracy. Moreover, while the dynamical model used for the controller synthesis requires high accuracy particularly in the frequency region of the 0 dB crossing of the loop gain, the required accuracy for the estimator model rather depends on the closed-loop feedback controller output. Once the feedback controller is designed, its output can be directly taken into account in the design of the topography estimator as a weighting in the data fitting:

$$\hat{G}(\omega, \theta) = \arg \min_{\hat{G}(\omega, \theta)} \sum_{\omega_f=\omega_1}^N \left[ \frac{[\hat{G}(\omega, \theta) - \Gamma(\omega_f)] \cdot K(\omega_f)}{1 + K(\omega_f) \cdot \Gamma(\omega_f)} \cdot V(\omega_f) \right]^2, (9)$$

with weighting filter  $V(\omega_f)$  capturing the expected frequency spectrum of the topography signal. Minimization of (9) can be done via the Sanathanan-and-Koerner method [Pintelon and Schoukens (2001)].

#### 4. DESIGN EXAMPLE AND ANALYSIS

In order to motivate the need for integrated design of the feedback controller and topography estimator, the procedure of Section 3 is demonstrated and analyzed in this section. The experimental setup used in this research is based on a commercially available AFM-system (Multimode V, Veeco, Santa Barbara USA), which utilizes a piezoelectric tube scanner to position the sample in all three spatial directions. This AFM-system is extended to a dual-actuated AFM by using a small piezoelectric plate actuator (CMAP12, Noliac, Kvistgaard, Denmark) which allows high bandwidth vertical positioning of the measurement tip. The dual-actuated setup allows a higher control bandwidth as compared to the single actuated setup, without sacrificing effective positioning range [Kuiper et al.

(2010)], and is shown schematically in Figure 3a. When considering integrated design of the feedback controller and topography estimator, the dual actuated system is especially interesting as the dynamical uncertainty of both actuators manifests differently and in different frequency regions, and the two actuators allow additional design freedom to cope with that. In this section, two different design cases are shown and compared with different emphasis on the topography estimation error.

##### 4.1 Design of feedback controller and topography estimator for dual actuated AFM-system

In order to identify the dynamical behavior of the system and its variations, the system is prepared several times with different measurement probes and sample discs, and the actuator responses are measured by using a network analyzer (4395A, Agilent, Santa Clara, USA). As this particular setup used in this research is typically used for high-speed contact-mode imaging, only measurement probes with high free resonance frequency cantilevers are considered, ranging from 300 kHz till 600 kHz. The weight of the sample discs used in these measurements range from 0.5 till 1 grams. The results of two different frequency response measurements for both actuators are shown in Figure 3b-c. From Figure 3b-c the first longitudinal resonance for the piezoelectric tube scanner can be recognized at 8 kHz, and for the piezoelectric plate actuator at 150 kHz. The various measurements, however, reveal some deviations in the dynamical behavior, which tends to become larger with increasing frequency. For the piezoelectric tube scanner (cf Fig. 3b) this can be recognized for instance at 1 kHz, which is the first lateral resonance mode of the tube, and after 10 kHz where the dynamical behavior is shown to be become very unpredictable. For the piezoelectric plate actuator, the dynamical behavior starts to show clear deviations after 50 kHz (cf Fig. 3c). Using the identification method described in Section 3.1, two 7th order dynamical models are fitted based on the frequency response data from the various measurement trails, which capture the nominal dynamical behavior of the system, and are shown in the dashed-dotted lines of Figure 3. Based on the nominal models the maximum multiplicative modeling error (cf. Eqn. (6)) is determined, and the over-bounding functions  $Q(s)$  are fitted, shown in the green and black-dashed lines of Figure 3b-c respectively.

Although not explicitly addressed during the identification experiments, both actuators are known to exhibit some hysteretic behavior which can cause a gain variation of about 5%. The hysteresis induced gain variation, however, is rather small as compared to the modeling error stemming from the uncertain dynamical modes at higher frequencies (cf. Fig. 3). Therefore, as for both actuators the over-bounding filters  $Q(s)$  are slightly conservative and have magnitudes above -26dB for all frequencies (i.e. corresponding to 5% deviation), the gain variation stemming from hysteresis is considered to be sufficiently captured in the uncertainty model as well.

The obtained system model is used for the design of the feedback controller using the method discussed in Section 3.2. To enforce the desired disturbance rejection characteristics of the closed-loop system, weighting filter  $W_e(s)$  (cf. Fig. 2) is shaped as an inverse high-pass filter. Critical

in the design of a feedback controller for a dual-actuated system is the frequency separation between both actuators, requiring the long-range actuator to primarily track the low-frequency topography variations, and the short-range actuator to take over at higher frequencies [Schroeck and Messner (1999)]. In order to obtain this frequency separation between both actuators, weighting filter  $W_u(s)$  (cf. Fig. 2) is used to enforce a low-pass behavior on the control action for the long-range actuator, and a bandpass behavior on the control action for the short-range actuator [Kuiper et al. (2010)]. The emphasis which is given on the quality of the topography estimation during the controller synthesis can be tuned via the weight  $W_{es}(s)$ . In order to analyze the consequences of taking the topography estimation problem directly into account when designing the feedback controller, two different feedback controllers and corresponding topography estimator are synthesized, using different static weights on the topography estimation error:  $W_{es}(s) = 1$ , and  $W_{es}(s) = 4$ . Given these weights on the topography estimation error, the weights on the control error  $W_e(s)$  and the controller outputs  $W_u(s)$  are tuned up to the point that the synthesis objective  $\gamma \leq 1$  (cf. Eqn. (8)) is just met. In both design cases two 30th order estimator models are fitted, based on the method discussed in Section 3.3, capturing the dynamics of both actuators for topography estimation.

#### 4.2 Performance Analysis

The synthesis results for both design cases are shown in Figures 4, 5, and 6. Figure 4 shows the resulting nominal sensitivity function  $E(s)/H(s)$  for both design cases, and Figure 5 shows the nominal complementary sensitivity function  $X(s)/H(s)$  for both cases. Figures 4, and 5 show that both the disturbance rejection bandwidth, as well as the tracking bandwidth is significantly lower in the case of  $W_{es}(s) = 4$ . The dashed lines in Figure 5 show the control actions of both actuators, showing that also the frequency at which the short-range actuator takes over from the long-range actuator is lower in the case  $W_{es}(s) = 4$ . Figure 6, on the other hand, shows the worst-case topography estimation error determined at each frequency point, by substituting the designed feedback controller  $K(s)$ , and estimator model  $\hat{G}(s)$ , and the data of the various frequency response measurements in (3):

$$\epsilon_{max}(\omega_f) = \max_{\substack{n \in [1 \dots j] \\ m \in [1 \dots k]}} \left| \frac{\begin{bmatrix} K_{lr}(\omega_f) \\ K_{sr}(\omega_f) \end{bmatrix}^T \begin{bmatrix} \Phi_{lr,n}(\omega_f) - \hat{G}_{lr}(\omega_f) \\ \Phi_{sr,m}(\omega_f) - \hat{G}_{sr}(\omega_f) \end{bmatrix}}{1 + \begin{bmatrix} K_{lr}(\omega_f) \\ K_{sr}(\omega_f) \end{bmatrix}^T \begin{bmatrix} \Phi_{lr,n}(\omega_f) \\ \Phi_{sr,m}(\omega_f) \end{bmatrix}} \right|,$$

with subscripts  $lr$  and  $sr$  denoting the long-range and short-range actuators, and  $j$  and  $k$  the amount of frequency responses measurements for the long-range and short-range actuator respectively. Figure 4 shows that with the lower bandwidth in the case  $W_{es}(s) = 4$ , also the worst-case topography estimation error is much lower as compared to the design case with  $W_{es}(s) = 1$ . This is explained by the fact that with a lower control bandwidth, also the excitation of the uncertain dynamics is lower, which improves the accuracy of the topography estimation. These results demonstrate that due to the uncertain actuator dynamics, a design trade-off can be made between the disturbance rejection bandwidth (i.e. the speed of the instrument), and the guaranteed bounds on the topography estimation error (i.e. the accuracy of the instrument).

To determine which one of the design cases might be better, the intended imaging applications of the instrument has to be considered. When imaging for instance fragile biological samples, minimizing the force variations between the tip and the sample may be most important in order not to damage the sample, and therefore the requirements on the accuracy of the topography estimation might be relaxed, aiming for an as high as possible control bandwidth. However, in other application like for instance in the semiconductor industry, higher emphasis might be given on the quality of the topography estimation, as the samples used in the semiconductor industry are most often much more firm, and higher importance may be given to the metrological aspects of the instrument.

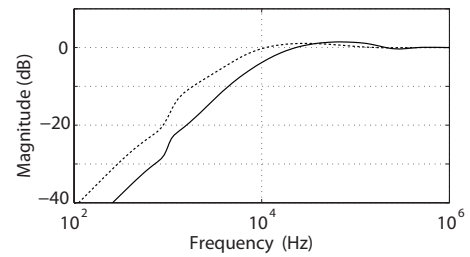


Figure 4. Bode magnitude plot of the nominal sensitivity function  $E(s)/H(s)$ , based on the feedback controllers designed with  $W_{es} = 1$  (solid), and  $W_{es} = 4$  (dashed).

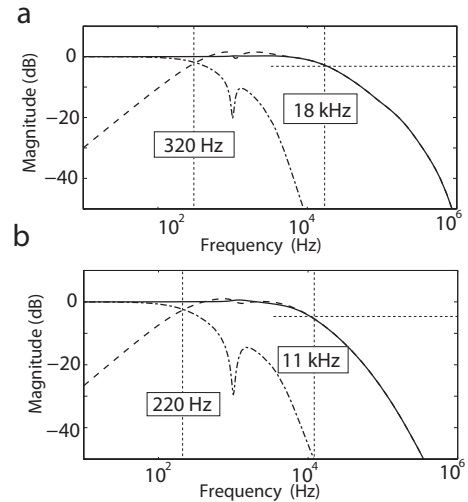


Figure 5. Bode magnitude plot of the nominal complementary sensitivity transfer of the system, based on the feedback controllers designed with  $W_{es} = 1$  (a), and  $W_{es} = 4$  (b). The dashed and the dashed-dotted lines show the contribution of the short-range, long-range actuator, respectively.

## 5. CONCLUSIONS

This contribution presents an integrated approach to design a robust feedback controller and topography estimator for the vertical feedback loop of a given AFM-setup, taking into account the dynamical uncertainties of the system. The proposed design approach is demonstrated on a prototype dual-actuated AFM-system, showing two different designs with different emphasis on the accuracy of the topography estimation. It is shown that due to the

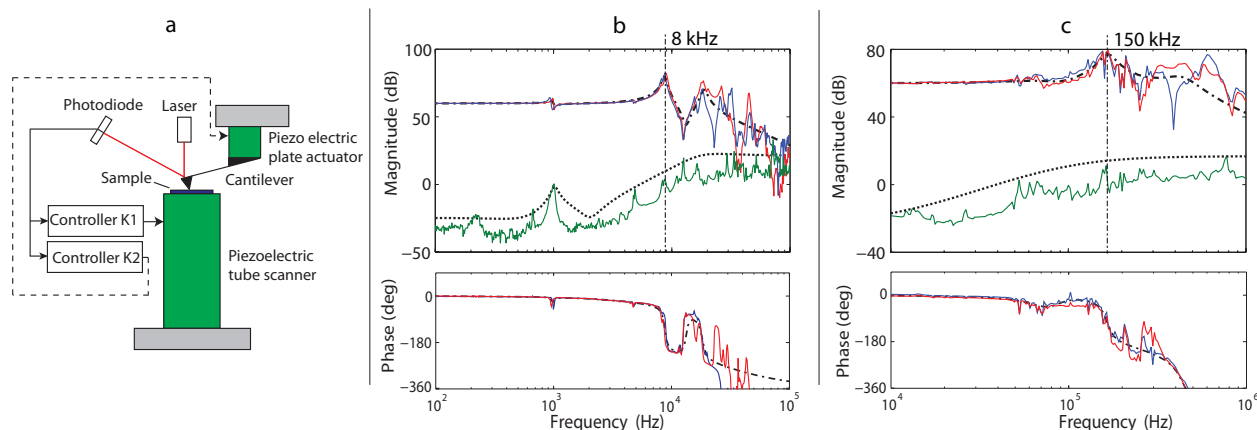


Figure 3. Schematic description of the dual actuated AFM (a), and frequency response of the tube scanner (b) and of the plate actuator (c), for two different measurement realizations (blue, and red), the 7th order model capturing the nominal dynamics (black, dashed-dotted), the maximum multiplicative model error (green), and the error over-bounding filter (black, dashed).

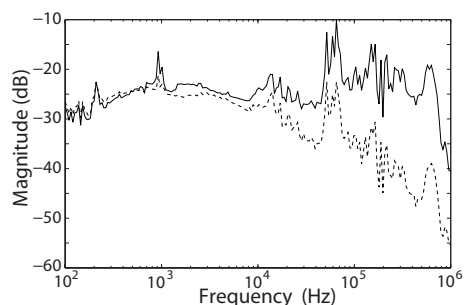


Figure 6. Worst-case topography estimation error determined at each frequency point for the closed-system designed with  $W_{es} = 1$  (solid), and  $W_{es} = 4$  (dashed).

presents of uncertain dynamical modes in the system, a trade off can be made between control bandwidth of the vertical feedback loop, and the accuracy of the topography estimation. These results suggest that when designing actuators for high-speed AFM, the actuator should not only be optimized for fast dynamics, but also the dynamical behavior should be consistent for the varying imaging conditions, to allow high-bandwidth control and accurate estimation of the sample profile at the same time.

## REFERENCES

- Ando, T., Kodera, N., Takai, E., Maruyama, D., Saito, K., and Toda, A. (2001). A high-speed atomic force microscope for studying biological macromolecules. *Proc. Nat. Acad. Sci.*, 98(22), 12468–12472.
- Binnig, G., Quate, C., and Gerber, C. (1986). Atomic force microscope. *Phys. Rev. Lett.*, 56(9), 930–933.
- Butterworth, J., Pao, L., and Abramovitch, D. (2009). A comparison of control architectures for atomic force microscopes. *Asian J. Control*, 11(2), 175–181.
- Devasia, S., Eleftheriou, E., and Moheimani, S. (2007). A survey of control issues in nanopositioning. *IEEE Trans. Control Syst. Technol.*, 15, p. 802–823.
- Douma, S. and Van den Hof, P. (2005). Relations between uncertainty structures in identification for robust control. *Automatica*, 41(3), 439–457.
- Hansma, P., Schitter, G., Fantner, G., and Prater, C. (2006). High speed atomic force microscopy. *Science*, 314, 601–602.
- Jeong, Y., Jayanth, G., Jhiang, S., and Menq, C. (2006). Direct tip-sample interaction force control for the dynamic mode atomic force microscopy. *Appl. Phys. Lett.*, 88, 204102.
- Kuiper, S., Fleming, A., and Schitter, G. (2010). Dual actuation for high speed atomic force microscopy. In *Proc. IFAC Mechatronics Conf. 2010*.
- Picco, L., Bozec, L., Ulcinas, A., Engledew, D., Antognozzi, M., Horton, M., and Miles, M. (2007). Breaking the speed limit with atomic force microscopy. *Nanotechnology*, 18, 044030.
- Pintelon, R. and Schoukens, J. (2001). *System identification: a frequency domain approach*. Wiley-IEEE Press.
- Salapaka, S., De, T., and Sebastian, A. (2005). A robust control based solution to the sample-profile estimation problem in fast atomic force microscopy. *Int. J. Robust Nonlin. Control*, 15(16), 821–838.
- Sarid, D. (1994). *Scanning Force Microscopy*. New York: Oxford Univ. Press.
- Schitter, G., Aström, K., DeMartini, B., Thurner, P., Turner, K., and Hansma, P. (2007). Design and modeling of a high-speed afm-scanner. *IEEE Trans. Control Syst. Technol.*, 15, 906–915.
- Schitter, G., Menold, P., Knapp, H., Allgöwer, F., and Stemmer, A. (2001). High performance feedback for fast scanning atomic force microscopes. *Rev. Sci. Instrum.*, 72, 3320.
- Schroek, S. and Messner, W. (1999). On controller design for linear time-invariant dual-input single-output systems. In *Proc. Am. Control Conf., 1999.*, volume 6.
- Skogestad, S. and Postlethwaite, I. (2005). *Multivariable feedback control: analysis and design*. John Wiley & Sons.
- Sulchek, T., Minne, S., Adams, J., Fletcher, D., Atalar, A., Quate, C., and Adderton, D. (1999). Dual integrated actuators for extended range high speed atomic force microscopy. *Appl. Phys. Lett.*, 75, 1637–1639.
- van Hulzen, J., Schitter, G., Van den Hof, P., and van Eijk, J. (2009). Load dynamics in piezoelectric actuation. In *Proc. Europ. Control Conf. 2009*.